Exp Fluids (2008) 45:501–511
DOI 10.1007/s00348-008-0493-5

RESEARCH ARTICLE

Determination of density and concentration from fluorescent images of a gas flow

Marco Belan · Sergio De Ponte · Daniela Tordella

Received: 22 June 2007 / Revised: 1 February 2008 / Accepted: 12 February 2008 / Published online: 28 March 2008

Abstract A fluorescence image analysis procedure to determine the distribution of species concentration and density in a gas flow is proposed. The fluorescent emission is due to the excitation of atoms/molecules of a gas that is intercepted by an electron sheet. The intensity of the fluorescent light is proportional to the local number density of the gas. When the gas flow is a mixture of different species, this proportionality can be used to extract the contribution associated with the species from the spectral superposition acquired by a digital camera. In particular, the fact is exploited such that the ratio between a pair of color intensities takes different values for different gases and that different linear superpositions of different color intensities yield a ratio that varies with the species concentration. This leads to a method that simultaneously reveals species concentrations and mass density of the mixture. For the proper working of a continuous electron gun in a gas, the procedure can be applied to gas flow where the pressure is below the thresholds of $200 \sim 300$ Pa and the number density is no greater than 10^{23} m^{-3}. To maintain the constancy of the emission coefficients, the temperature variation in the flow should be inside the range 75–900 K (above the temperature where the probability to meet disequilibrium phenomena due to rarefaction is low, below the temperature where visible thermal emission is present). The overall accuracy of the measurement method is approximately 10%. The uncertainty can vary locally in the range from 5 to 15% for the concentration and from 5 to 20% for the density depending on the local signal-to-noise ratio. The procedure is applied to two under-expanded sonic jets discharged into a different gas ambient—Helium into Argon and Argon into Helium—to measure the concentration and density distribution along the jet axis and across it. A comparison with experimental and numerical results obtained by other authors when observing under-expanded jets at different Mach numbers is made with the density distribution along the axis of the jet. This density distribution appears to be self-similar.

M. Belan · S. De Ponte
Dipartimento di Ingegneria Aeronautica e Spaziale,
Politecnico di Milano, Milan, Italy

D. Tordella (✉)
Dipartimento di Ingegneria Aeronautica e Spaziale,
Politecnico di Torino,
International Collaboration for Turbulence Research,
Turin, Italy
e-mail: daniela.tordella@polito.it

1 Introduction

The density measurement technique in gas flows performed by means of an electron beam was described extensively by Muntz (1968) in an early review, that also reported the first attempts to obtain species concentration using filters in the optical system.

Electron beam techniques were also well described by Bütefisch and Vennemann (1974).

Later on, spectral measurements were performed on gas flows excited by an electron beam. These measurements yielded concentration and density values in isolated points in space.

Cattolica et al. (1979) presented a work on mixed monoatomic gases in which point measurements of density, temperature, and velocity were determined from electron beam fluorescence measurements. Later, Cattolica (1988) presented experiments on the use of an electron beam and laser-induced fluorescence in high speed flows, where the

concentration of nitric oxide was measured by means of spectroscopic methods. Another spectral study of the fluorescent emission of nitrogen, helium, and nitric oxide in a hypersonic wind tunnel along with an analysis of background noise effects was reported by Price et al. (1992). Recent reviews in this field, which include the electron beam technique and species concentration measurement in hypersonic flows, have been written by Dankert et al. (1993) and Gochberg (1994). The applicability of relevant methods has also been discussed for hot gases in high enthalpy flows, and at relatively high densities. The extension of the electron-beam techniques to higher density-and-temperature test flows is possible, thanks to the introduction of the pulsed electron beam—that replaces the continuous one—which was first obtained by Lutfy and Muntz (1999); see also the recent work by Wehrmeyer (2006).

The electron-beam measurements that have been found in the literature are usually carried out at isolated spatial points. These measurements are usually very accurate for spectral scales, i.e., the gas emission is often analyzed for each single spectrum line. Other techniques, such as high-speed rainbow schlieren deflectometry (RSD), are more effective in reconstructing flow spatial evolution as they allow instantaneous concentration contours to be determined across the field (Alammar et al. 1998; Agrawal et al. 2002; Yildirim and Agrawal 2005).

Laser techniques can be very efficient and accurate in measuring concentrations and velocities in many flows. They, however, require depending on the particular method employed, seeding of some kind. The fluid seeding—in case liquid or solid particles are used—must behave as a passive scalar, which is a major problem in conditions of gas flows relatively rarefied as are those met in highly compressible situations. As an alternative, lasers that are tuned on characteristic emission lines of the gases involved in the experiment must be employed. A complete review on laser-based diagnostic techniques in hypersonic flows, compared with electron beam techniques, can be found in Grisch (2000).

The experimental technique herein described aims at the simultaneous measurement of the distribution of the species concentration and density in sections of a gas flow crossed by an electron sheet. The measurement is based on the analysis of fluorescent images obtained through gas ionization induced by an electron beam and acquired by a classic Charge Coupled Device (CCD) camera. As such it can be a fast and low-cost method to obtain simultaneous concentration and density maps on the whole image. Since it requires only a common CCD camera, it can be considered alternative or preliminary with respect to the use of spectrometric devices. The signal obtained from the color CCD yields, within each pixel, the projection of the fluorescence spectrum on three wavelength bands relevant to the standard colors red, green and blue (RGB). By means of suitable data post-processing, the data collected from a camera image are transformed into concentration and density maps. The aim is to obtain fast and simultaneous measurements on a large section of the test flow. The technique is applied here to the measurement of axial and transversal density and concentration distributions in under-expanded hypersonic gas jets issued into a different gas ambient. The work is organized as follows. The experimental equipment and the test flow are described in Sect. 2. Section 3 presents the data analysis algorithm. Section 4 contains the results and discussion. The concluding remarks are given in Sect. 5.

2 Experimental set-up and test flow characteristics

The study and implementation of the present technique are carried out in an apparatus designed for the study of hypersonic jets (Belan et al. 2001, 2004). In this study, the flows under test are underexpanded jets obtained from truncated sonic nozzles and flowing along the longitudinal axis of a cylindrical vacuum vessel. The vessel is modular, with a total length of 5 m and a diameter of 0.5 m. The diameter of the orifice of the nozzles ranges from 0.3 to 2 mm; the vessel diameter is thus much larger than the diameter of the jets. As a consequence, the wall effects are limited. The apparatus is shown in Fig. 1, where the 3-module configuration is represented (up to five sections can be mounted). The vessel is equipped with a system of valves for the control of both the jet issued by the nozzles and the ambient gas. An electron gun operating at very low pressures, thanks to a set of secondary pumps, and a color CCD camera can be mounted onto several ports and optical windows.

The stagnation pressure p_0 of the jets (at $T = 300\ K$) can be varied in the range from 2,000 to 2×10^5 Pa. The

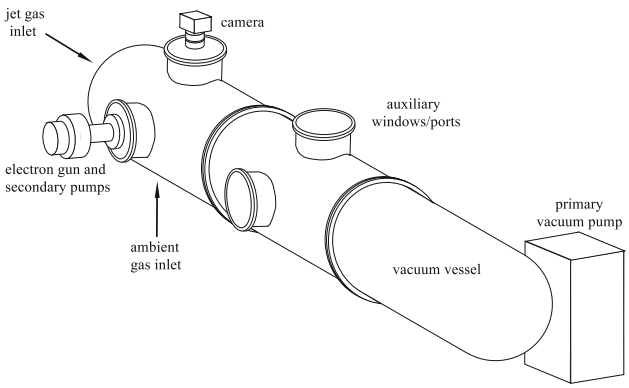

Fig. 1 Experimental apparatus. The vacuum vessel is shown in the three-section configuration; two extra sections are available

pressure in the vessel can be adjusted from 1.5 to 200 Pa by varying the volume flow of the primary vacuum pump. The resulting stagnation/ambient pressure ratio, p_0/p_{amb}, ranges over 5 orders in magnitude. Stagnation pressures are measured by a 1% accuracy instrument ranging from 10^3 to 10^5 Pa, whilst pressures in the vessel are monitored by means of 0.25% accuracy transducers, ranging from 0.01 to 10 Pa and from 0.1 to 100 Pa.

In this experiment, it is possible to use different gases for the jet and the surrounding ambience in the vessel. This allows variation of the density ratio ρ_{jet}/ρ_{amb} (where ρ_{jet} is the long-term jet density far from the nozzle) as an independent parameter. The density ratio in the far field can range from 0.04 to 45 for jet/ambient gas pairs chosen from air, Helium, Argon and Xenon.

The jets are characterized by the presence of a barrel shock and a normal shock (Mach disk) in the near field—the flow region close to the nozzle exit. In some configurations the presence of secondary expansions and recompressions can be observed beyond the first Mach disk (Belan et al. 2004, 2006). In this experiment, the Mach number of the jets upstream of the disk is very high; values of up to 30 can be obtained. The Knudsen number K, based on the mean free path of gases in equilibrium conditions and on the jet diameter, always remains in the continuum regime, except for particular cases (when the jet gas is helium with a high p_0/p_{amb} ratio, K may approach the value of 0.5 in a small region upstream of the Mach disk).

The time scale of the flow is defined as the time necessary for a fluid particle to cover the length of the vacuum chamber, which is of the order of 1 ms. The system permits an outflow of hundreds of time scales (typically 0.5 s). Since the primary pump has a very large delivery, the jet evolution can be considered quasi-steady.

The experimental setup is shown in Fig. 2. The electron gun is operated at 16 kV, with currents of up to 2 mA, and

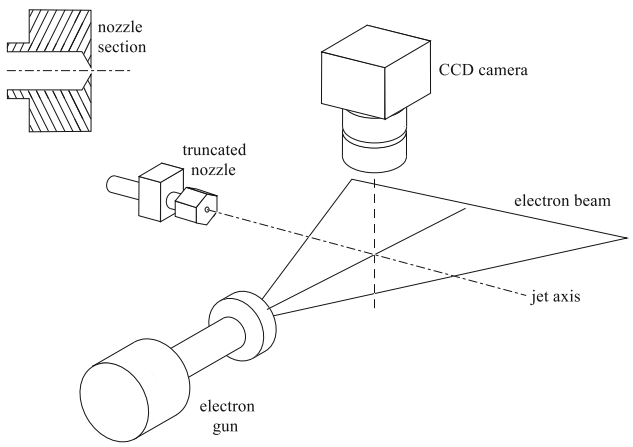

Fig. 2 Experimental setup. The truncated convergent nozzle is sonic at the exit section. The nozzle is here shown in the *upper left corner* is equipped with a deflection system that creates an electron sheet. The sheet intercepts the jet, and generates a plane fluorescent section of the flow, which is then acquired by a high sensitivity camera (1 megapixel CCD with Bayer RGB filter).

This arrangement makes it possible to visualize the jet over many spatial scales, usually up to 200 initial diameters. An important feature of the experiment is the possibility of studying the effect of two main flow control parameters (the ambient/jet density ratio, and the Mach number) that can be set independently from each other. Through the visualization of slices of the flow, and through the determination of the relevant density and species concentration distribution, it is possible to obtain information about the mixing layer and the thickness of the shocks.

The present technique is subject to the conditions of proper working of a continuous electron gun in a gas, that is a gas number density approximately no greater than 10^{23} m^{-3} (for example, the best working range for air at ambient temperature $T = 300\ K$ is $n < 2 \times 10^{22}$ m^{-3}, which is equivalent to a mass density $\rho < 2$ g/m^3, or a pressure $p < 300$ Pa).

3 A new procedure for the determination of density and concentration spatial distribution from fluorescent images

The present method is based on the fluorescent emission from a gas excited by an electron beam. The relation between the radiation intensity I and the number density n of a gas (Brown and Miller 1957) is

$$I = \frac{k\,n}{1 + h\,n} \tag{1}$$

where k is a constant that includes the sensitivity of the measuring system, and h is a specific coefficient of the nature of the gas which depends on the temperature ($h = 2\sigma^2 P_{jk}^{-1}\sqrt{4\pi R_{gas} T}$, where σ is the quenching collision diameter, P_{jk} the spontaneous transition probability, T the temperature and R_{gas} the gas constant). Fluorescence occurs when the molecules excited by the electrons return to the ground state and give back energy in the form of emitted light. The energy of incident electrons can also be transferred to translational molecular degrees of freedom or other molecular excited states (quenching collisions). In relation (1), the $k\,n$ factor accounts for the proper fluorescence phenomenon, whilst the term hn in the denominator accounts for the loss of fluorescence caused by quenching.

For relatively rarefied gases, that is, those in the small number density limit, Eq. (1) shows that I is proportional to n, whilst for higher densities, the emission encounters an asymptotic limit (saturation):

$$I \propto n \quad \text{as} \quad n \to 0 \tag{2}$$

$$\lim_{n\to\infty} I = \text{const.} \tag{3}$$

At the low pressures considered here ($1.5 < p < 200$ Pa), Eq. (1) can be approximated as

$$I = k\, n, \tag{4}$$

The structure of this last relation implies that k—being a constant—is independent from the thermodynamic variables, the temperature and pressure. Within this structure, in fact, the dependence on these variables of the fluorescent emission is accounted for through the proportionality with the numerical density. The limits of validity of this formulation are the following: (i) The temperature of the gas is so high to be in the presence of a visible emission ($T > 900$ K). (ii) If the gas is a mixture, the density is not low enough to give a decoupled emission (which would mean that the intensity of the light emission of one single species is not independent from that of the other species, so that the mixture emission is not given by the sum of the partial intensities of the different species). (iii) In highly rarefied flow conditions, when the temperature is very low (few degrees Kelvin) and several nonequilibrium phenomena may appear as, for example, the molecular aggregations in gases which are monoatomic at room temperature, see Hillard et al. (1970), Cattolica et al. (1974). In this regard, a precautionary lower limit for the temperature can be a value of about 75 K.

The above conditions are not encountered in the most part of the underexpanded jets observed in this work. In fact, the gas temperature is always equal or less than the ambient temperature ($\sim$300 K) and the number density is lower than 10^{23} m^{-3}. However, the region close to the nozzle exit is to be excluded because there, at the beginning of the expansion, the density is still too high, and thus there is saturation of the emission and relation (4) is not yet valid. Furthemore, the region of maximum expansion preceding the Mach disk can be cold and rarefied. To be on the safer side, one can consider properly to exclude also this region. However, a posteriori, we have verified in this region a good constrast with results coming from other laboratory and numerical experiments; see Sect. 4 and Fig. 12 for details.

A check on the temperature dependence associated with the coefficient h in (1) can also be made. For instance, in the case of Helium it can be observed that for large n (i.e., $>10^{24}$), such that (3) is going to be valid, and in the hypothesis of constant atomic cross-section, a variation of the temperature from 300 K to 100 K yields a variation in the ratio between the intensity I coming from the complete equation (1) and I_{lin} coming from the linearized equation (4) which is less than 5%. It should be noted that such conditions of simultaneous high density and cold gas are never met in the present experiments.

Since I is a spectral superposition, Eq. (4) also holds for the three colors acquired and stored in the digital image yielded by the camera. Three values depending on the spectral emission range associated with each color must then be introduced: in this study, we adopt the well-known RGB codification (R = red, G = green, B = blue, see Fig. 3). Thus, it is possible to write

$$R = k_R n \tag{5}$$

$$G = k_G n \tag{6}$$

$$B = k_B n, \tag{7}$$

where the constants k_R, k_G, k_B are integral quantities that can be computed from known spectra or directly measured.

The k-parameters in the laws of kind $I = k\, n$ are obtained from experimental calibrations in a known gas. By filling the vacuum vessel with a pure gas and keeping it at rest, with stable pressure p and temperature T, it is possible to read a pair of values I,p. The repetition of this procedure with various pressures p_i at the same T gives an array of pairs $\{I_i,p_i\}$. The perfect gas law yields the numerical density $n = p\mathcal{N}_A/(\mathcal{R}T)$ (where $\mathcal{N}_A$ and $\mathcal{R}$ are the Avogadro

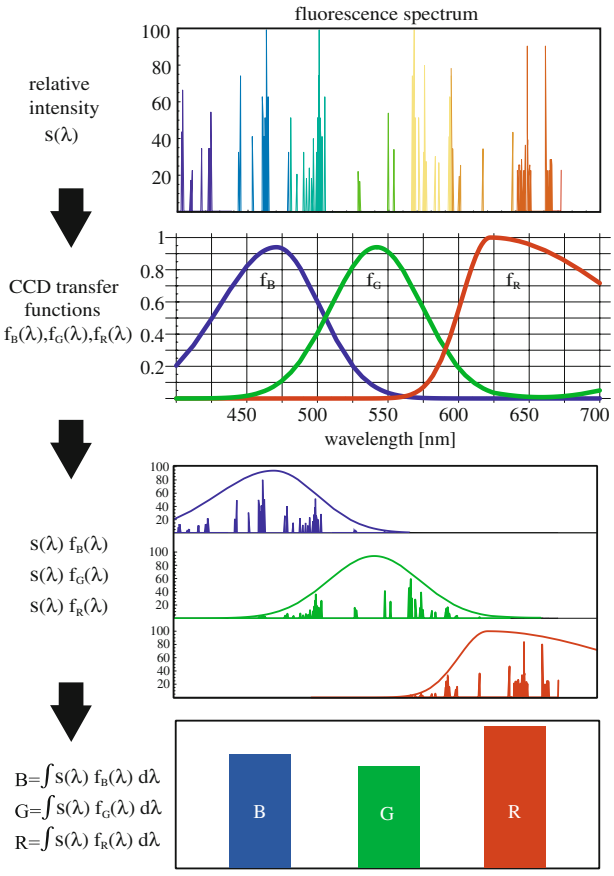

Fig. 3 Fluorescent emission acquired by an RGB sensor: the spectral lines are projected onto the RGB response curves of the CCD. The plots are normalized to maximum values

number and the universal gas constant, respectively). Thus, an array of values $\{I_i,n_i\}$ is obtained; k-parameters are then deduced through a linear fit, and the relevant uncertainties can be calculated accounting for the noise levels in the original fluorescent signal and the other sources of experimental errors.

Figure 4 shows the calibration values for pure Helium and pure Argon, measured at $T = 297 \pm 0.5$ K. The k-parameters obtained from the data in Fig. 4 are the following, given in (pixel values)/m^3:

$$k_{R,\mathrm{He}} = (2.160 \pm 0.073) \times 10^{-20}$$
$$k_{G,\mathrm{He}} = (1.147 \pm 0.063) \times 10^{-19}$$
$$k_{B,\mathrm{He}} = (2.151 \pm 0.022) \times 10^{-19}$$
$$k_{R,\mathrm{Ar}} = (1.085 \pm 0.017) \times 10^{-18}$$
$$k_{G,\mathrm{Ar}} = (7.406 \pm 0.333) \times 10^{-19}$$
$$k_{B,\mathrm{Ar}} = (1.273 \pm 0.017) \times 10^{-18}$$

Uncertainties of k-constants are obtained by propagation of errors, accounting for calibration images noise, temperature and pressure uncertainties and data dispersion with respect to the fits.

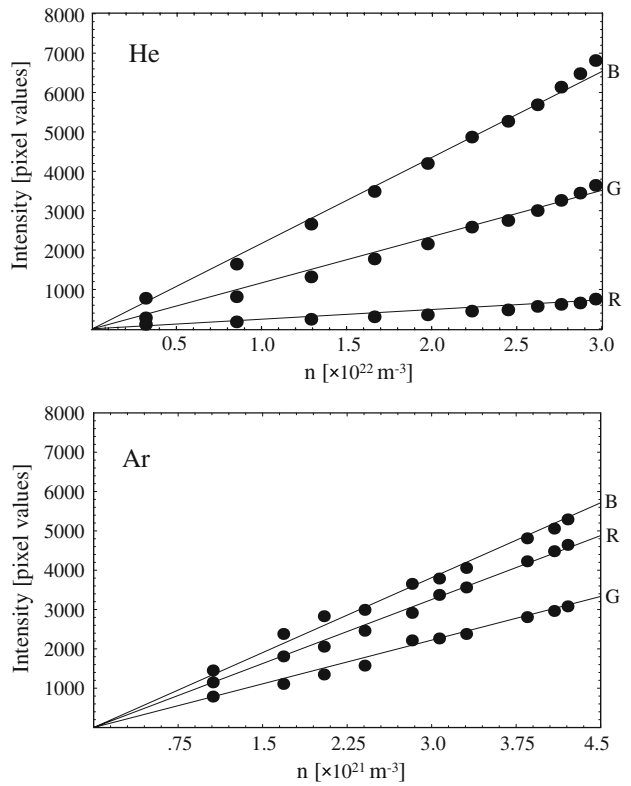

Fig. 4 Fluorescent emission acquired using an RGB sensor and varying the number density of the gas. The slopes of these curves are the constants k_R, k_G, k_B in Eqs. (5–7)

It should be noted that for any linear superposition of fluorescent emissions,

$$C = aR + bG + cB, \tag{8}$$

one obtains:

$$C = (ak_R + bk_G + ck_B)n = k_C n. \tag{9}$$

This relation also holds for a two-gas mixture. If the mixture is sufficiently rarefied to consider the radiation emission of the two gases as decoupled, the total intensity will be the sum of the individual ones. The present method assumes that this condition is satisfied.

If the ambient gas is labeled with 'amb' and the jet gas with 'jet', the fluorescence emission C can be written as a sum of two expressions of the kind (9):

$$C = C_{\mathrm{amb}} + C_{\mathrm{jet}} = k_{\mathrm{amb}}n_{\mathrm{amb}} + k_{\mathrm{jet}}n_{\mathrm{jet}} \tag{10}$$

By using again Eq. (9) we obtain

$$k_C n = k_{\mathrm{amb}}n_{\mathrm{amb}} + k_{\mathrm{jet}}n_{\mathrm{jet}} \tag{11}$$

By dividing by the total numerical density n and introducing the concentrations $z_{\mathrm{amb}} = n_{\mathrm{amb}}/n$ for the ambient gas and $z_{\mathrm{jet}} = n_{\mathrm{jet}}/n$ for jet gas, the following is obtained

$$k_C = k_{\mathrm{amb}}z_{\mathrm{amb}} + k_{\mathrm{jet}}z_{\mathrm{jet}}, \tag{12}$$

where

$$k_a = ak_{R\mathrm{amb}} + bk_{G\mathrm{amb}} + ck_{B\mathrm{amb}}, \tag{13}$$
$$k_j = ak_{R\mathrm{jet}} + bk_{G\mathrm{jet}} + ck_{B\mathrm{jet}}. \tag{14}$$

It should be noticed that the ratio between a pair of color intensities takes different values for different gases. For example, the electron beam ionization at 16 kV of pure helium in the pressure range 0.1 Pa $< p <$ 200 Pa at 300 K gives an outstanding spectral line at 501 nm, whilst in the same conditions pure Argon gives a wide spectrum with several lines of comparable intensity, particularly in the red and blue zones. In this case, for example, the ratio R/G will take on low values for helium and high values for Argon.

Two linear superpositions of the kind

$$C_1 = a_1R + b_1G + c_1B \tag{15}$$
$$C_2 = a_2R + b_2G + c_2B \tag{16}$$

will usually give a ratio C_1/C_2 that varies with the species concentration. A suitable choice of the six coefficients a_i,b_i,c_i $(i = 1,2)$ can be made in order to obtain a ratio C_1/C_2 that varies over the largest possible interval for a given pair of gases, which in turn leads to the concentration determination.

In order to obtain a relation between the ratio C_1/C_2 and the concentration z of a gas species, C_1/C_2 must be rewritten using Eqs. (9) and (12):

$$\frac{C_1}{C_2}=\frac{k_{C1}}{k_{C2}}=\frac{k_{\mathrm{amb}_1}z_a+k_{\mathrm{jet}_1}z_{\mathrm{jet}}}{k_{\mathrm{amb}_2}z_a+k_{\mathrm{jet}_2}z_{\mathrm{jet}}}. \tag{17}$$

The concentrations of the two gases are linked by the relationships $z_{\mathrm{amb}}=1-z_{\mathrm{jet}}$. Imposing $C_1/C_2=r$, Eq. (17) becomes

$$r=\frac{k_{\mathrm{amb}_1}\left(1-z_{\mathrm{jet}}\right)+k_{\mathrm{jet}_1}z_{\mathrm{jet}}}{k_{\mathrm{amb}_2}\left(1-z_{\mathrm{jet}}\right)+k_{\mathrm{jet}_2}z_{\mathrm{jet}}}. \tag{18}$$

By solving with respect to z_{jet}, one obtains

$$z_{\mathrm{jet}}=\frac{k_{\mathrm{amb}_1}-k_{\mathrm{amb}_2}r}{k_{\mathrm{amb}_1}-k_{\mathrm{jet}_1}+\left(k_{\mathrm{jet}_2}-k_{\mathrm{amb}_2}\right)r}. \tag{19}$$

This gives the concentration in the jet gas, for each pixel of the image, as a function of the ratio r of the two superpositions C_1, C_2, and as a function of the four constant k_{amb1}, k_{amb2}, k_{jet1}, k_{jet2}. These constants are defined through Eqs. (13, 14) and can be determined when the constants $k_{R\mathrm{amb}}$, $k_{G\mathrm{amb}}$, $k_{B\mathrm{amb}}$, $k_{R\mathrm{jet}}$, $k_{G\mathrm{jet}}$ and $k_{B\mathrm{jet}}$ are known and the six coefficients a_i,b_i,c_i, $i=1,2$ are set for a given pair of gases. In practice, the r variable is the ratio of the emission intensities measured in each pixel of the image for the two selected superpositions.

The four constants $k_{\mathrm{amb}_1},k_{\mathrm{amb}_2},k_{\mathrm{jet}_1},k_{\mathrm{jet}_2}$ are not independent, since, by means of Eq. (17), it is possible to write the following for the pure ambient gas ($z_{\mathrm{amb}}=1$, $z_{\mathrm{jet}}=0$) and for the pure jet gas ($z_{\mathrm{amb}}=0$, $z_{\mathrm{jet}}=1$)

$$\frac{C_{\mathrm{amb}_1}}{C_{\mathrm{amb}_2}}=\frac{k_{\mathrm{amb}_1}}{k_{\mathrm{amb}_2}}\quad;\quad\frac{C_{\mathrm{jet}_1}}{C_{\mathrm{jet}_2}}=\frac{k_{\mathrm{jet}_1}}{k_{\mathrm{jet}_2}} \tag{20}$$

so that

$$k_{\mathrm{amb}_1}=k_{\mathrm{amb}_2}\frac{C_{\mathrm{amb}_1}}{C_{\mathrm{amb}_2}}\quad;\quad k_{\mathrm{jet}_1}=k_{\mathrm{jet}_2}\frac{C_{\mathrm{jet}_1}}{C_{\mathrm{jet}_2}}. \tag{21}$$

Equation (19) can thus be written in the form

$$z_{\mathrm{jet}}=\frac{A-r}{(A-r)-M(J-r)} \tag{22}$$

where r is the independent variable (obtained from each image pixel, using the chosen set of coefficients a_1, b_1, c_1 and a_2, b_2, c_2), $A=C_{\mathrm{amb}_1}/C_{\mathrm{amb}_2}$ is a known constant for the pure ambient gas, $J=C_{\mathrm{jet}_1}/C_{\mathrm{jet}_2}$ is a known constant for the pure jet gas, $M=k_{\mathrm{jet}_2}/k_{\mathrm{amb}_2}$ is a ratio of known constants that are separately determined and are associated with the triplet $a_2,b_2,c_2(k_{\mathrm{jet}_2}=a_2k_{R\mathrm{jet}}+b_2k_{G\mathrm{jet}}+c_2k_{B\mathrm{jet}}$ and $k_{\mathrm{amb}_2}=a_2k_{R\mathrm{amb}}+b_2k_{G\mathrm{amb}}+c_2k_{B\mathrm{amb}})$. The constants A,J and M are calculated from the known k-constants. Equation (22) is a hyperbolic law which is physically meaningful for values of z_{jet} in the range $0\le z_{\mathrm{jet}}\le 1$, corresponding to a range $r_{\min}<r<r_{\max}$.

Once the concentrations are known, the density can be determined, as the total number density n may be obtained from relations such as (9), e.g., one can use

$$C_1=k_{C_1}n,\quad k_{C_1}=k_{\mathrm{amb1}}z_{\mathrm{amb}}+k_{\mathrm{jet1}}z_{\mathrm{jet}} \tag{23}$$

or

$$C_2=k_{C_2}n,\quad k_{C_2}=k_{\mathrm{amb2}}z_{\mathrm{amb}}+k_{\mathrm{jet2}}z_{\mathrm{jet}}. \tag{24}$$

The density is finally given by the equation

$$\rho=n(z_{\mathrm{amb}}m_{\mathrm{amb}}+z_{\mathrm{jet}}m_{\mathrm{jet}}) \tag{25}$$

where m_{amb}, m_{jet} are the molecular masses of the gases in the ambient and in the jet, respectively.

It is worth noting that since the values of $r=C_1/C_2$ are obtained from the image analysis, the image noise may lead to z_{jet} values that lie outside the physical range. The noise is particularly troublesome when it induces a value r close to the value $r_s=(MJ-A)/(M-1)$ that is a singularity of Eq. (22), which however lies outside the physical domain $r_{\min}<r<r_{\max}$.

The noise effects are sketched in Fig. 5. It should be noted that it is advisable to adopt a noise filtering technique in the image post-processing. In particular, the filter must preserve the primary ratios among the three colors R, G and B along the image.

It should also be noticed that this procedure does not work well when the fluorescence spectra of the ambient gas and the jet gas are similar (for example air and Argon). The constants A and J become nearly equal, the constant M becomes nearly equal to unity and as a consequence the concentration measurement becomes impossible in this case.

The present measurements are always performed on 1,300 × 1,030 RGB images, with a 10-bit resolution. Images were obtained by operating the electron gun at 16 kV with a beam current of 1.5 mA.

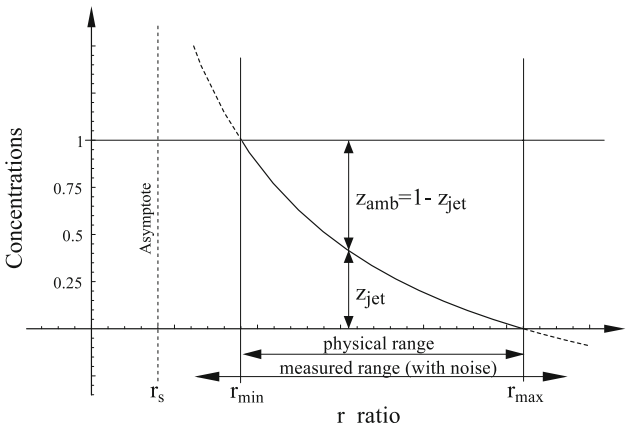

Fig. 5 Typical dependence of the concentration z on the color ratio r. The measured range of the variable r is usually larger than the physical range because of noise

4 Results and discussion

The procedure was applied to measure the concentration z and the density ρ in two underexpanded jets. The first is a jet of Helium in an Argon ambient where the jet gas density is less than the ambient gas density (*under-dense* jet) and the relevant pressure ratio p_0/p_a is 0.84×10^3. The second is a jet of Argon in a Helium ambient where the jet gas density is greater than the ambient gas density (*over-dense* jet) and the pressure ratio is 1.2×10^3. The exposure time was 1/12 s, that is a lapse of time much longer than the flow time scale (about 1 ms), but shorter than the outflow time, which is ~ 0.5 s. Thus, each image can be assumed to visualize the flow in quasi-steady conditions. The images are compensated for the nonuniformity of the electron sheet, and filtered to improve the signal-to-noise ratio by means of local averages in small neighborhoods of each pixel.

As a first example, the Helium jet flowing in an Argon ambient is considered. The choice of the coefficients in this case is $a_1 = 1$, $b_1 = 1$, $c_1 = 1$; $a_2 = 0$, $b_2 = 1$, $c_2 = 0$. Then, the known k-values are used to calculate the coefficients in Eq. (22), leading to:

$$A = C_{a1}/C_{a2} = 4.18 \pm 0.14 \quad \text{for pure Ar (ambient gas)},$$
$$J = C_{j1}/C_{j2} = 3.06 \pm 0.11 \quad \text{for pure He (jet gas)},$$
$$M = k_{j2}/k_{a2} = 1.58 \pm 0.06 \quad \text{for the He--Ar pair (jet/ambient)}$$

where the uncertainties are obtained by error propagation. The physical range for r, see Fig. 5, is in this case $3.06 < r < 4.18$.

Figure 6 shows the Helium jet obtained with a stagnation pressure $p_0 = (3.06 \pm 0.20) \times 10^4$ Pa, whilst the pressure of the Argon ambient is $p_a = 36.5 \pm 0.5$ Pa. The figure is strongly contrasted for clarity. The measurements are performed along the x-axis and along two cross-sections, section A before the Mach disk and section B after the disk. It should be noticed that the Knudsen number upstream of the Mach disk in this jet is quite high, about 0.5. This explains why the shock is very thick.

Figure 7a shows the concentration curves of this jet at the cross-sections A ($x/d = 17.6 \pm 0.5$) and B ($x/d = 26.4 \pm 0.5$). The radial distance is nondimensionalized by the initial jet diameter $d = 2$ mm, which is the diameter of the nozzle orifice. The uncertainties are obtained by propagation of errors in Eq. (22), where the variance of coefficients A, J, M is known (see text above) and the uncertainty of r comes from noise values along the image. The amplitude $2\sigma_z$ of error bars is truncated when it exceeds physical limits (i.e., when $z + \sigma_z > 1$). The highest helium concentration is on the jet axis and the lower concentrations are in the outer zone. In particular, the curves show that the mixing with the ambient is more effective after the shock, as the helium concentration increases after the Mach disk.

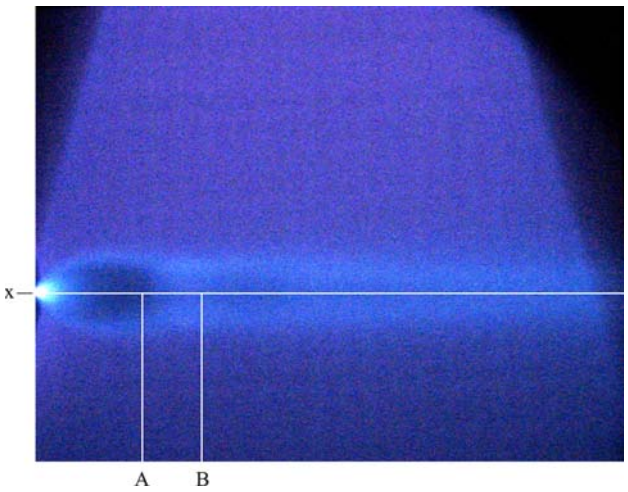

Fig. 6 Helium jet in an Argon medium: pressure ratio $p_0/p_a \sim 0.84 \times 10^3$, Mach before the normal shock ~ 26, Reynolds number at the nozzle exit = 3,000. The straight lines (A, B) mark the measurement sections

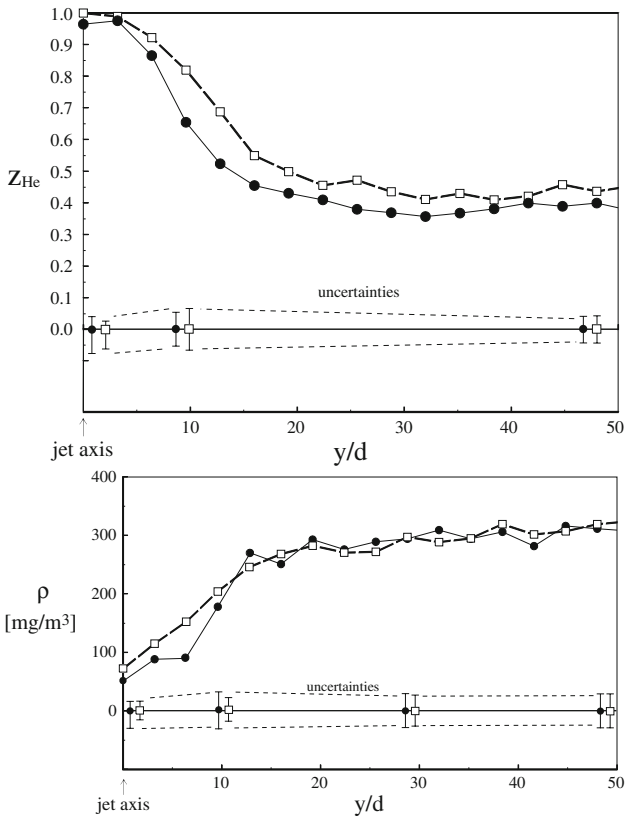

Fig. 7 He jet in an Ar ambient, see visualization in Fig. 6, $p_0/p_a = 0.84 \times 10^3$, Mach before the normal shock ~ 26, nozzle exit Reynolds number = 3,000. **a** Cross-sectional concentration. **b** Cross-sectional density. *Filled circle* section (A), before the Mach disk. *Open square* section (B), after the Mach disk

Figure 7b shows the density distributions. This is the total density obtained from Eq. (25). It can be seen that the jet remains under-dense with respect to the surrounding

ambient even in the post-shock zone. Uncertainties are obtained by propagation of errors in Eq. (25), which gives the amplitude $2\sigma_z$ of error bars. Error bars on the (A) curve have been intentionally overestimated for $y/D < 10$. Actually, the very strong expansion present in that region could yield nonequilibrium conditions and spectrum variations at very low T. To be on the safer side, we considered as a reference limit value the ρ value pertaining to an ideal isentropic expansion with the same pressure ratio p_0/p_a. The good comparison we have a posteriori observed with results obtained by other researchers using different techniques (either laboratory or numerical simulation technique, see Fig. 12) confirm that this uncertainty is overestimated.

Figure 8 shows the axial density and He concentration in the jet (the first point on the left of the curves is omitted because of image saturation). It can be seen that the shock thickness is remarkable. The density measured after the shock is close to the ideal one, but the density measured before the shock is greater than the ideal (isoentropic) one, because the strong expansion effects are probably as such to yield their nonequilibrium conditions. In this jet, it is also possible to see secondary expansions and compressions after the Mach disk. The uncertainty on the concentration and the density is obtained as previously described for Fig. 7.

The shock center location is estimated as $x_M = (21.7 \pm 0.5)d$, which is in good agreement with the theoretical shock position given by Young (1975)

$$x_M = C_\gamma d\sqrt{p_0/p_a} \tag{26}$$

where C_γ is a constant that depends on the specific heat ratio of the gas in the jet, in this case $C_\gamma = 0.76$ and $p_0/p_a = 0.84 \times 10^3$, which gives $x_M/d = 22.01$. The shock thickness Δ is of the order of $11d$. The concentration of Helium is equal to 1 at the nozzle exit and remains almost constant along the axis. Mild oscillations in phase with that of the density are observed downstream of the Mach disk.

According to Ashkenas et al. (1966) and Young (1975), the maximum Mach number before the shock can be estimated as $M_{\max} \simeq 26$ at $x = x_M$. This is obtained through a semi-empirical model which assumes that the rapid expansion downstream of the nozzle exit is isentropic and that the streamline in the region of the flow inside the barrel shock satisfies spherical symmetry close to the axis.

The second test case is the Argon jet flowing in a Helium ambient. This jet could be considered as the complementary configuration of the previous case. The exchange of gases in the jet and in the ambient produces an over-dense jet in place of the preceding under-dense case. The choice for the six coefficients a_i, b_i, c_i, $i = 1,2$ of the algorithm is the same as that of the previous test case. The ambient gas/jet gas exchange yields

$$A = 3.06 \pm 0.1$$
$$J = 4.18 \pm 0.1$$
$$M = 0.63 \pm 0.06.$$

Figure 9 shows a visualization image of the Argon jet, which is flowing in similar conditions to those applied to the complementary jet visualized in Fig. 6, because the stagnation/ambient pressure ratio is of the same order ($p_0/p_a = 1.2 \times 10^3$). Here, the stagnation pressure is $p_0 = (5.68 \pm 0.20) \times 10^4$ Pa, and the helium ambient pressure is $p_a = (45.7 \pm 0.5)$ Pa. As in the previous case, the measurements are performed along the x-axis and along two cross-sections A and B.

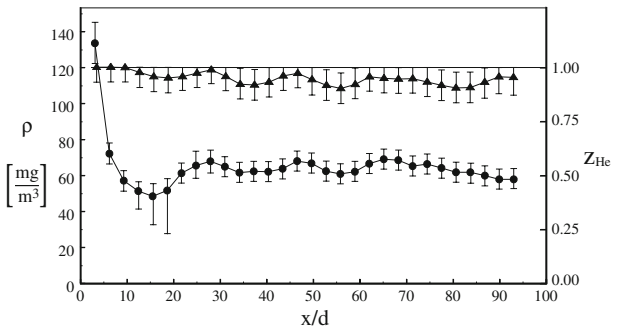

Fig. 8 Axial concentration and density for the Helium jet visualized in Fig. 6, $p_0/p_a = 0.84 \times 10^3$, Mach before normal shock ~ 26, Reynolds number at the nozzle exit = 3,000. *Filled circle* density, *open triangle* concentration. It should be noted that the *error bars* in the range $10 < x/d < 20$ are estimated assuming as a reference an isentropic expansion (spherical symmetry, thermodynamic equilibrium), which leads to an overestimation of the errors, see text in Sects. 3 and 4 and Fig. 12

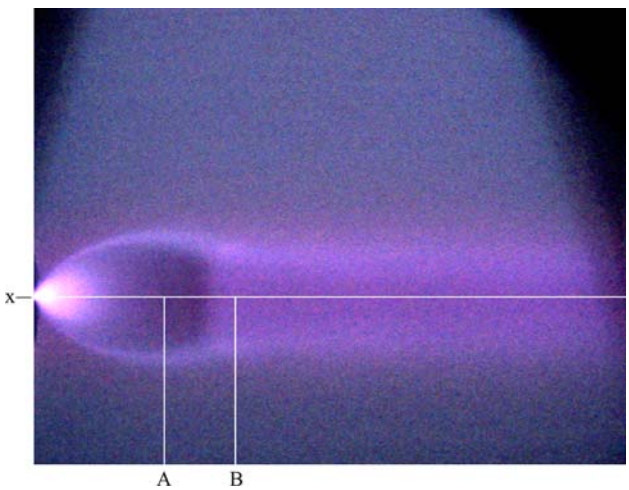

Fig. 9 Argon jet in a Helium medium: pressure ratio $p_0/p_a = 1.2 \times 10^3$, Mach before the normal shock ~ 29, Reynolds number at the nozzle exit = 18,200. The *straight lines* (*A*,*B*) indicate the cross-stream measurement sections

Figure 10a shows the concentration curves of this jet at the cross-sections A ($x/d = 20.5 \pm 0.5$) and B ($x/d = 30.7 \pm 0.5$). As in the former case, uncertainties are obtained by error propagation in Eq. (22); the amplitude of error bars is truncated when it exceeds physical limits. In this case, the diffusion of the gas, the heavy Argon, in the surrounding ambient is very effective. In fact, the Argon concentration in the ambient is larger than 0.7 throughout. In the Helium jet case, the lateral far field concentration of Helium was 0.4. The lateral spreading of the jet is also larger, and is of the order of 35–40 nozzle exit diameters compared to the 20 diameters found for the Helium jet. Figure 10b shows two cross-sectional density curves of the same jet, as in Fig. 10a. Here, the jet is always over-dense and remarkably so in the mixing layer zone. The uncertainty is obtained as in the former flow configuration case.

Figure 11 shows the axial density and Ar concentration distributions in this jet. Also in this case the density measured after the shock is close to the ideal one, but the density measured before the shock is greater than the ideal (isentropic) one, because the strong expansion effects are probably as such to set nonequilibrium conditions in that zone. Nevertheless, there is a good a posteriori comparison with results obtained by other researchers using different techniques, see Fig. 12. The uncertainty is obtained as in the former flow configuration case (Helium jet in Argon ambient), and is overestimated in the region preceding the normal shock.

In this case, the shock is thinner ($<3d$). The concentration of the gas along the jet axis in this case is again almost constant. The mild oscillations in the z curve are of the order of computed uncertainties and not correlated to oscillations in the ρ curve. Thus, it cannot be concluded that there are further expansions or compressions downstream as in the former case. The estimated shock center location $x_M = (27 \pm 0.5)\ d$ is in good agreement with the prediction $x_M = 26.8\ d$ given by Eq. (26) with a pressure ratio $p_0/p_a = 1.2 \times 10^3$(constant C_γ is again equal to 0.76 because Ar and He are both monatomic). The estimate of the maximum Mach number upstream of the shock is 29.

The discussion of the results can be completed by presenting, in Fig. 12, a comparison with results obtained by other researchers using very different methodologies, such as a numerical simulation of an Argon jet in an Argon ambient based on Euler's equations (Nishida et al. 1985), a numerical simulation of an air jet in air based on the Monte Carlo direct simulation method (D'Ambrosio et al. 1999), and laboratory laser interferometer measurements of an Argon jet in an Argon ambient (Kobayashi et al. 1984). A simple $1/r^2$ expansion is also included among the other curves. The compared jets are characterized by different values of two control parameters, the Reynolds number (in

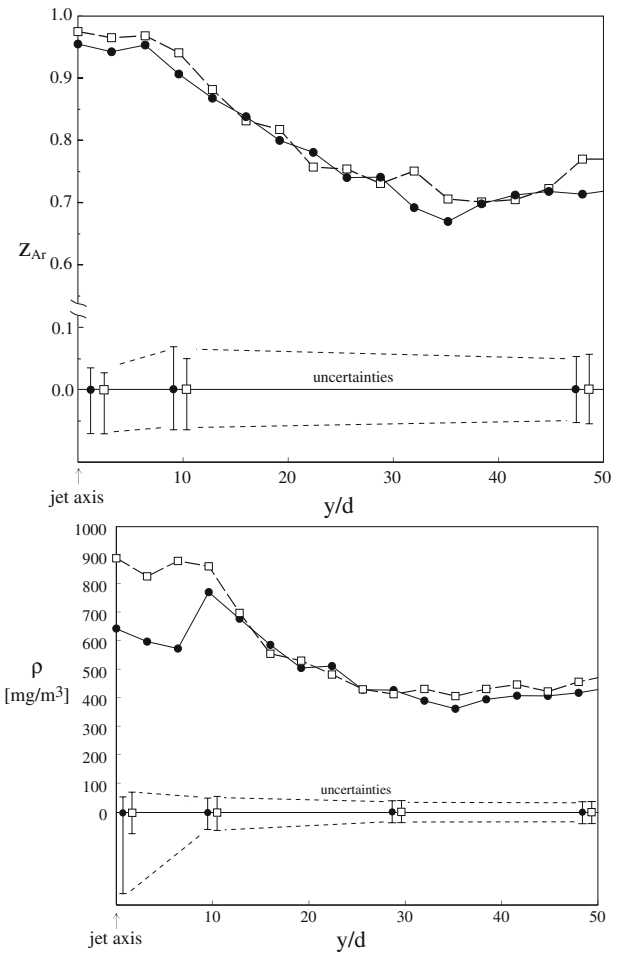

Fig. 10 Argon jet in a Helium ambient, see visualization in Fig. 9, $p_0/p_a = 1.2 \times 10^3$, Mach before the normal shock $\sim$29, Reynolds number at the nozzle exit = 18,200. **a** Cross-sectional concentration. **b** Cross-sectional density. *Filled circle* before the Mach disk. *Open square* after the Mach disk

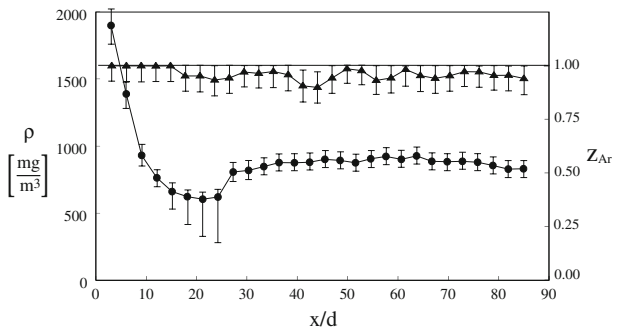

Fig. 11 Axial concentration and density in the Argon jet, see visualization in Fig. 9, $p_0/p_a = 1.2 \times 10^3$, Mach before the normal shock $\sim$29, Reynolds number at the nozzle exit = 18,200. *Filled circle* density; *open triangle* concentration. It should be noted that the *error bars* in the range $15 < x/d < 25$ are estimated assuming as a reference an isentropic expansion (spherical symmetry, thermodynamic equilibrium), which leads to an overestimation of the errors, see text in Sects. 3 and 4 and Fig. 12

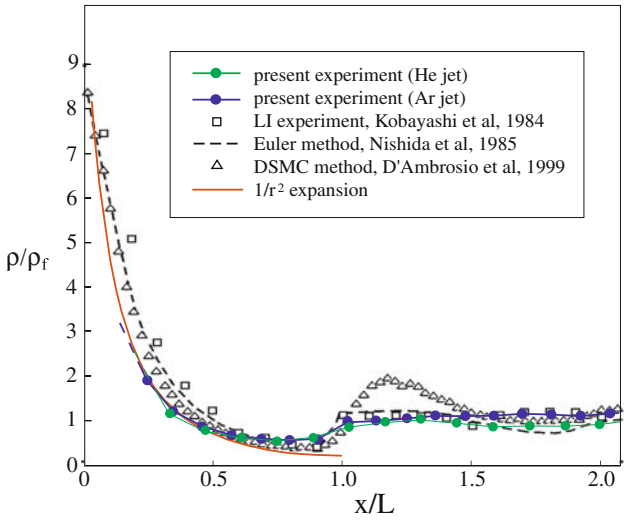

Fig. 12 Comparison of the streamwise axial density distribution in different under-expanded jets. *Green circles* He in Ar, $Re = 3{,}000$, $M = 26$. *Blue circles* Ar in He, $Re = 18{,}200$, $M = 29$. *open square* $Re = 3{,}800$, $M = 6.7$. *Dashed line* Ar in Ar, $Re = 3{,}800$, $M = 6.7$. *Triangle* air in air, $M = 5$. *Red line* $M = 29$. M is the maximum Mach number in the jet which is encountered in front of the Mach disk, Re is the Reynolds number at the sonic nozzle exit

particular the Re based on flow values at the sonic nozzle exit) and the Mach number reached before the normal shock. It can be noticed that the axial densities collapse very well on a single self-similar curve far from the nozzle, which is obtained by scaling the longitudinal distance with the axial length of the barrel shock L and by scaling the density with the value reached beyond the normal shock. This comparison shows that the present density determination procedure from fluorescent images is effective. From the dynamical point of view, this result has highlighted the Reynolds and Mach number similarity of the intermediate field of under-expanded jets.

If we exclude the rarefied region before the normal shocks, where an overestimation of the uncertainty can be only presented, the overall accuracy of these measurements is about 10%. The uncertainty can vary locally in the range from 5 to 15% for the concentration and from 5 to 20% for the density depending on the local signal-to-noise ratio. Additional data are available for the case of jets consisting of the same gas as the ambient; in that case the accuracy in density measurements can improve to overall values less than 5%.

5 Conclusions

We propose a new procedure to exploit the information included in the fluorescent image of a gas in motion to determine the distribution of species concentration and density. The fluorescent emission is produced by the excitation of atoms/molecules of the gas when an electron sheet crosses it. The intensity of the fluorescent light is proportional to the local number density of the gas. When the gas flow is a mixture of different species, this proportionality allows the contribution associated with different chemical species from the spectral superposition acquired by a digital camera to be determined. This yields a means of simultaneously obtaining species concentration and mass density in gas mixture flows. The procedure was applied to two underexpanded gas jets discharged into a different gas ambient—Helium into Argon and Argon into Helium. The obtained density distributions compare satisfactorily with other experimental and numerical determinations.

The limits of the present measurements are essentially linked to the saturation of the emission intensity at high densities and to the poor signal-to-noise ratio at very low densities. In the underexpanded jets tested here, the limits only pertain to a very small region close to the sonic nozzle (where density is very high and the density would be underestimated) and to a small zone upstream of the Mach disk (where density is very low and the measured values are overestimated with respect to the values deduced in case the assumption of thermodynamic equilibrium is retained). In the high-density zone, also the measured concentration could differ from the theoretical unitary value because of the saturation of the RGB colors. However, a comparison with results obtained from other authors on under-expanded jets with different values of Mach and Reynolds numbers is found to be very satisfactory. One result associated with the validation analysis of the present procedure was the confirmation that the longitudinal evolution of an under-expanded jet becomes almost self-similar in the far zone when scaling the streamwise coordinate with the barrel shock length.

The results considered here show that this technique could be useful in measuring mixing layer thicknesses, as the mixing region between the jet and the surrounding ambient is in the best working range for this algorithm. This suggests that the technique may be used in other gas flows with shear layers, provided the fluorescent spectra of the gases are sufficiently different.

The present technique is not limited to applications pertaining to highly compressible flows. In fact, gas flows that are incompressible, but stratified in density and/or species concentration, can be considered provided the pressure remains below a threshold of about $200 \sim 300$ Pa (depending on the gas nature).

References

Agrawal AK, Alammar KN, Gollahalli SR (2002) Application of rainbow schlieren deflectometry to measure temperature and oxygen concentration in a laminar gas–jet diffusion flame. Exp Fluids 32:689–691

Alammar K, Agrawal AK, Gollahalli SR, Griffin D (1998) Application of rainbow schlieren deflectometry for concentration measurements in an axisymmetric helium jet. Exp Fluids 25:89–95

Ashkenas H, Sherman FS (1966) The structure and utilization of supersonic free jets in low density wind tunnels. In: de Leeuw JH (ed) Rarefied gas dynamics. Academic, New York, pp 84–105

Belan M, Tordella D, De Ponte S (2001) A system of fast acceleration of a mass of gas for the laboratory simulation of stellar jets. In: 19th ICIASF, Cleveland

Belan M, De Ponte S, Massaglia S, Tordella D (2004) Experiments and numerical simulations on the mid-term evolution of hypersonic jets. Astrophys Space Sci 293(1–2):225–232

Belan M, De Ponte S, Tordella D (2006) Simultaneous density and concentration measurements on hypersonic jets, Abstract, EFMC6 KTH. In: Euromech fluid mechanics conference 6, Royal Institute of Technology, Stockholm

Brown LO, Miller N (1957) α-Ray induced luminescence of gases. Trans Faraday Soc 53:748

Bütefisch KA, Vennemann D (1974) The electron-beam technique in hypersonic rarefied gas dynamics. Prog Aerosp Sci 15:217–255

Cattolica RJ (1988) Advanced optical diagnostics in hypersonic research. In: Summary of discussions at the 11th meeting of the Sandia cooperative group on the aerothermochemistry of turbulent combustion, USA, vol 42

Cattolica RJ, Robben F, Talbot L, Willis DR (1974) Translational nonequilibrium in free jet expansions. Phys Fluids 17(10):1793–1807

Cattolica RJ, Gallagher R, Anderson JB, Talbot L (1979) Aerodynamic separation of gases by velocity slip in free jet expansions. AIAA J 17(4):344–355

D'Ambrosio D, De Socio LM, Gaffuri G (1999) Physical and numerical experiments on an under-expanded jet. Meccanica 34:267–280

Dankert C, Cattolica R, Sellers W (1993) Local measurement of temperatures and concentrations: a review for hypersonic flows. AGARD, theoretical and experimental methods in hypersonic flows 10

Gochberg LA (1994) The electron beam fluorescence technique in hypersonic aerothermodynamics. In: AIAA, 18th aerospace ground testing conference, Colorado Springs, CO, USA

Grisch F (2000) Molecular diagnostics for the study of hypersonic flows. ONERA report. Dept. Mesures Physiques, Chatillon, France

Hillard ME, Ocheltree SL Storey RW (1970) Spectroscopic analysis of electron-beam-induced fluorescence in hypersonic helium flow. NASA technical note TN D-6005

Kobayashi H, Nakagawa T, Nishida M (1984) Application of laser interferometry to density measurements in free jets. Trans Jpn Soc Aerosp Sci 27:184–192

Lutfy FM, Muntz EP (1999) Spectroscopic survey of gases found in hypersonic flows using pulsed electron beam fluorescence. In: 35th AIAA/ASME/SAE/ASEE joint propulsion conference and exhibit, Los Angeles, CA, USA

Muntz EP (1968) The electron beam fluorescence technique, AGARDograph 132

Nishida M, Nakagawa T, Kobayashi H (1985) Density contours of a supersonic free jet. Exp Fluids 3:181–183

Price L, Williams WD, Powell HM (1992) Electron beam fluorescence measurements in the Boeing hypersonic shock tunnel. In: NASA Langley Research Center, The 1992 NASA Langley Measurement Technology Conference: measurement technology for aerospace applications in high-temperature environments, pp 305–320

Wehrmeyer JA (2006) Pulsed electron beam spectroscopy of N_2^+ for temperature and density measurement. In: 44th AIAA aerospace sciences meeting and exhibit, Reno, Nevada, USA

Yildirim BS, Agrawal AK (2005) Full-field measurements of self-excited oscillations in momentum-dominated helium jets. Exp Fluids 38:161–173

Young WS (1975) Derivation of the free-jet Mach disk location using the entropy-balance principle. Phys Fluids 18(11):1421–1425